J. Fluid Mech. (2010), *vol.* 654, *pp.* 473–500.
doi:10.1017/S0022112010000479

Homogeneity of turbulence generated by static-grid structures

Ö. ERTUNÇ[1]†, N. ÖZYILMAZ[2], H. LIENHART[1], F. DURST[3] AND K. BERONOV[1]

[1]Lehrstuhl für Strömungsmechanik, Universität Erlangen-Nürnberg, Cauerstraße 4, D-91058 Erlangen, Germany

[2]Institut für Technische Mechanik, TU-Clausthal, Adolph-Roemer-Strae 2A D-38678 Clausthal-Zellerfeld, Germany

[3]Centre of Advanced Fluid Mechanics, FMP Technology GmbH Am Weichselgarten 34 D-91058 Erlangen, Germany

(Received 25 November 2008; revised 19 January 2010; accepted 25 January 2010; first published online 11 May 2010)

Homogeneity of turbulence generated by static grids is investigated with the help of hot-wire measurements in a wind-tunnel and direct numerical simulations based on the Lattice Bolztmann method. It is shown experimentally that Reynolds stresses and their anisotropy do not become homogeneous downstream of the grid, independent of the mesh Reynolds number for a grid porosity of 64 %, which is higher than the lowest porosities suggested in the literature to realize homogeneous turbulence downstream of the grid. In order to validate the experimental observations and elucidate possible reasons for the inhomogeneity, direct numerical simulations have been performed over a wide range of grid porosity at a constant mesh Reynolds number. It is found from the simulations that the turbulence wake behind the symmetric grids is only homogeneous in its mean velocity but is inhomogeneous when turbulence quantities are considered, whereas the mean velocity field becomes inhomogeneous in the wake of a slightly non-uniform grid. The simulations are further analysed by evaluating the terms in the transport equation of the kinetic energy of turbulence to provide an explanation for the persistence of the inhomogeneity of Reynolds stresses far downstream of the grid. It is shown that the early homogenization of the mean velocity field hinders the homogenization of the turbulence field.

1. Introduction

Grid-generated turbulent flows have been the subject of numerous turbulence investigations due to their statistical properties, among them the invariance of all statistical moments to translation, i.e. its presumed homogeneity. Owing to the translational invariance of homogeneous turbulence, decay processes in undistorted flows and the effects of mean velocity distortion on this kind of turbulent flows have constituted the framework of understanding and modelling of turbulent flow phenomena. In experimental investigations, homogeneous turbulence has commonly been produced by static-grid structures. The generated turbulence is not spatially homogeneous in the flow direction, because it decays in this direction or is modified

† Email address for correspondence: ertunc@lstm.uni-erlangen.de

under the influence of constant mean velocity gradient, i.e. mean velocity distortion. However, the changes in the flow direction are treated as changes in time for a Lagrangian fluid element using Taylor's frozen turbulence assumption (see for example Batchelor 1953).

The research work of Taylor (1935*a*, 1937, 1938), von Kármán (1937) and von Kármán & Howarth (1938) represents pioneering studies investigating homogeneous and nearly isotropic turbulence. Batchelor & Townsend (1948*a*, 1948*b*) showed that the decay of nearly isotropic grid-generated turbulence is composed of initial, transition and final periods. Batchelor & Townsend (1949) investigated the spectrum of decaying nearly isotropic grid turbulence to determine the ranges of wavenumbers in which the small-scale eddies are in equilibrium as proposed by Kolmogorov (1941*a*, 1941*b*). Comte-Bellot & Corrsin (1966, 1971) produced turbulence with improved isotropy by slightly contracting the grid-generated turbulence. Their investigations revealed that the normal turbulent stresses behind a static grid have a power-law decay in the initial and the transition periods. The coefficients of the power-law decay were later investigated by many researchers, e.g. Naudascher & Farell (1970), Mohamed & Larue (1990), and more recently Lavoie, Djenidi & Antonia (2007) and Mazellier & Vassilicos (2008).

The effects of the fundamental types of distortions on homogeneous turbulent flows, i.e. strain, shear and rotation, constituted a central area of turbulence research which was expected to reveal the interaction between the mean and the fluctuating motion. The first investigations date back to Prandtl (1932, 1933) and Taylor (1935*b*), both of whom studied the effect of wind-tunnel contraction on the free stream turbulence. Townsend (1954) systematically investigated the effect of irrotational uniform distortion without streamwise strain on homogeneous turbulence. Tucker & Reynolds (1968) and Reynolds & Tucker (1975) extended these investigations on irrotational distortion of homogeneous turbulence. They studied a range of distortion scenarios: plane strain, symmetric contraction and flattening contraction. The studies of Uberoi (1956), Mills & Corrsin (1959), Tan-atichat, Nagib, & Drubka (1980), Warhaft (1980) and Sjögren & Johansson (1998) also investigated the effect of axisymmetric contraction applied to nearly isotropic turbulence generated by static grids. Gence & Mathieu (1979) considered two successive plain strains without streamwise acceleration of the velocity.

The relaxation of anisotropic homogeneous turbulence is another important type of homogeneous turbulence. The turbulence was made to be anisotropic by either axisymmetric strain or plain strain. After straining, the mean velocity distortion was switched off, so that the effect of viscous dissipation and the slow part of the pressure-strain correlations of anisotropic turbulent fluctuations could be investigated isolated from the mean flow distortion. Uberoi (1956, 1957) and Mills & Corrsin (1959) were the first to observe that the anisotropic turbulence, which was generated by an axisymmetric contracting nozzle, tended to become isotropic while it was decaying. Therefore, this behaviour of turbulence is called the 'return-to-isotropy'. The anisotropic flows generated by plain strain were experimentally investigated by Tucker & Reynolds (1968), and more recently by Gence & Mathieu (1980). In general, these experimental studies showed that the decrease in anisotropy is essentially controlled by the type of anisotropy generated. Warhaft (1980) and Choi & Lumley (2001) also carried out investigations on the return-to-isotropy problem.

Homogeneous pure shear turbulence and pure rotation turbulence have also been studied by many researchers. Among the homogeneous turbulent flows, pure shear flows are the most relevant to the turbulent boundary layer flows. Hinze (1975,

chapter 4) gave a good insight into homogeneous shear flows. More recently, Shen & Warhaft (2000, 2002), Warhaft & Shen (2002) and Ferchichi & Tavoularis (2000) questioned the local isotropy of turbulence formulated by Kolmogorov (1941*a*) in pure shear turbulence. In contrast to the postulate of local isotropy, they showed that the small-scale turbulence can be anisotropic even at high turbulence Reynolds numbers and large-scale structures do not stop interacting with small-scale structures with increasing turbulence Reynolds numbers. The review of Gence (1983) or the book of Sagaut & Cambon (2008) on homogeneous turbulence should be referred to for a more complete overview of homogeneous turbulence.

In order to ensure the homogeneity of the turbulent flow field in the wake of a grid, Corrsin (1963) suggested three conditions that should be satisfied. First, the porosity of the grid, which is the ratio of open to total area of the grid structure, should be large enough to prevent coalescing jets and large-scale instability downstream of the grid. Corrsin (1944) studied unstable jet coalescence downstream of two-dimensional jets. Based on his observations and the available literature, he suggested the existence of a critical porosity value above which unstable jet coalescence does not occur. von Bohl (1940) revealed that critical porosity might lie between 54 % and 63 %. Bradshaw (1964, 1965) suggested that porosity should be larger than 57 % to avoid instabilities and Tan-atichat & Nagib (1982) suggested 60 % and 70 % for grids and screens, respectively. Second, the diameter or the height of the flow duct, say D, must be much larger than the length scale of the energy-containing eddies, which is of the same order as the mesh size of the grid (M), i.e. $D/M \gg 1$. In other words, the larger the ratio D/M, the smaller is the effect of the walls on the measured data to be expected. Third, the measurements should be taken far downstream, since the turbulence becomes homogeneous only after at least 40 mesh sizes downstream of the grid. Lack of one or more of these conditions might lead to inhomogeneity and, therefore, the resultant data must not be compared with the laws deduced for homogeneous turbulence. In other words, after fulfilling these conditions, measurements of undistorted and distorted grid-generated turbulence were expected to reflect the properties of homogeneous turbulence.

Most of the above-mentioned studies have satisfied these conditions. However, to the best of the authors' knowledge, there have been only a few studies that directly investigated the homogeneity of the grid-generated turbulence. Batchelor & Townsend (1948*a*, 1948*b*) and Batchelor & Stewart (1950) recognized the lack of homogeneity for very fine grids (grids of 1/4 inch mesh size). Grant & Nisbet (1957) showed that the inhomogeneity of Reynolds stresses can reach up to ± 15 % at $x_1/M = 80$ for a mesh size of 1/4 inch and ± 6 % at $x_1/M = 30$ for a 2 inch mesh size. All their grids had a porosity of 70 %, i.e. much larger than the value suggested by Bradshaw (1964, 1965). Moreover, their transverse profile measurements in the wake of the grids showed wavy r.m.s. values of turbulent velocity fluctuations. Their investigations revealed that, with increasing mesh size, the inhomogeneity dropped. Moreover, they showed that the location of the measurement axis along the flow direction has a drastic effect on the decay of grid turbulence. In detailed studies on turbulence manipulators, Loehrke & Nagib (1972) and Tan-atichat & Nagib (1982) also measured standing wavy structures. In a study by Liu, Ting & Rankin (2004), the inhomogeneity of the r.m.s. of velocity fluctuations increased in the streamwise direction, reaching up to 30 % at $x_1/M = 40$ for perforated plates of 65 % porosity. They showed that the higher the solidity, the greater is the inhomogeneity of the r.m.s. of velocity fluctuations. The literature shows that although grid-generated turbulence was utilized in many experimental turbulence investigations, its homogeneity did

Re_M/Porosity	53 %	64 %	72 %	82 %
1400	DNS-LBGK ($17 < Re_\lambda < 11$)	DNS-LBGK ($15 < Re_\lambda < 10$)	DNS-LBGK[a,b] ($14 < Re_\lambda < 9$)	DNS-LBGK ($13 < Re_\lambda < 7$)
4000		EXP. ($34 < Re_\lambda < 18$)		
5333		EXP. ($50 < Re_\lambda < 24$)		
8000		EXP. ($74 < Re_\lambda < 36$)		

TABLE 1. The mesh Reynolds number Re_M, turbulence Reynolds number Re_λ and porosity in the experimental and numerical simulations. The Re_λ ranges in experimental cases (EXP.) are given for $16 \leqslant x_1/M \leqslant 110$ and in numerical simulations they are given for $10 \leqslant x_1/M \leqslant 50$.
[a]An extra simulation with a computational domain of size $2400 \times 400 \times 400$ was made.
[b]An extra simulation with a non-uniform grid was made.

not attract enough interest and, consequently, was mostly accepted as an *ad hoc* assumption.

Recently, Ertunç (2007) conducted detailed hot-wire measurements in the wake of a grid of 64 % porosity at different Reynolds numbers. He found that turbulence generated by punched grids showed wavy transverse profiles of Reynolds stresses far downstream of the grid ($x_1/M > 30$), similar to those observed by Grant & Nisbet (1957), despite the fact that the porosity of the grid employed was higher than those suggested in the literature (Bradshaw 1964, 1965; Tan-atichat & Nagib 1982). As the grid structures employed in those experiments had a 1.3 % standard deviation of porosity, i.e. they were slightly non-uniform, it was not clear whether the non-uniformity caused the observed inhomogeneity in Reynolds stresses. Hence these findings triggered our efforts to conduct direct numerical simulations (DNS) of grid-generated turbulence by using the standard Lattice Boltzmann BGK method (LBGK). The present paper summarizes these results and carries out a comparison with the experiments.

The main objectives of this study were to determine the extent of homogeneity in the flow field, the dependence of homogeneity on the grid Reynolds number and the porosity of the grid structure and its non-uniformity. The research also considers the reasons for the persistence of the Reynolds stress inhomogeneity far downstream of the grid. Hence the investigations presented here cover grid porosity ranging from 53 to 83 % and grid Reynolds numbers from 1400 to 8000, as listed in table 1. The Reynolds number effect on the homogeneity of turbulence quantities is shown via measurements, and DNS is employed to show the effects of porosity and grid non-uniformity and to analyse the time-averaged dynamics of turbulence behind the static grids.

2. Grid-Generated turbulence in the wind tunnel

2.1. *Flow facility and instrumentation*

The effect of the grid Reynolds number on the homogeneity of grid-generated turbulence was investigated experimentally. For the measurements of turbulence downstream of a static-grid structure, the closed-loop, low-speed wind tunnel at LSTM-Erlangen was employed (figure 1). The open test section of the wind tunnel was almost completely closed to prevent the generation of free shear turbulence at the edges of the flow in the test section and its influence on the measurements. The closed part of the test section was 1.8 m in width, 1.4 m in height and 2 m in length.

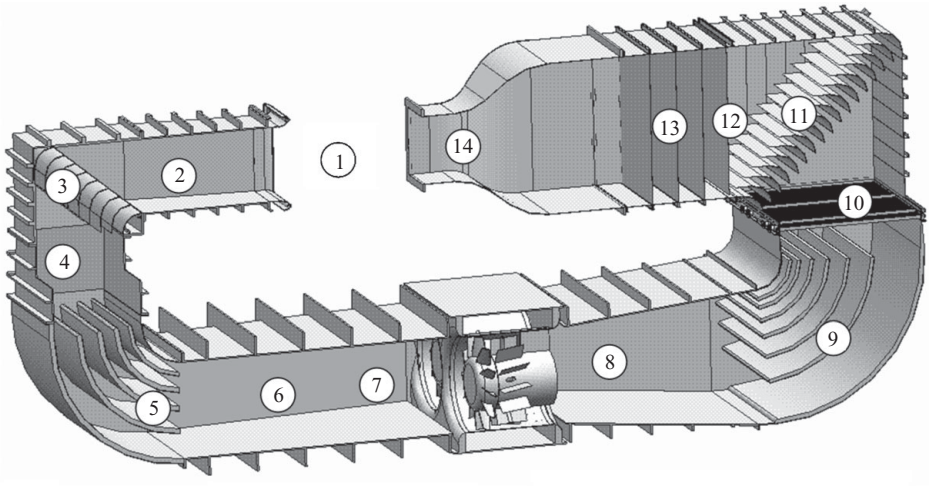

(1) Test section
Length = 2800 mm
Height = 1400 mm
Breadth = 1866 mm
U_{max} = 55 m s^{-1} (open)
U_{max} = 60 m s^{-1} (closed)

(2) (4) (6) Diffuser
(3) (5) (9) (11) Turning vanes
(7) Axial fans (2×)
(10) Heat exchanger
(12) Honeycomb
(13) Wire screens (3×)
(14) Contraction (5:1)

FIGURE 1. The closed-loop wind tunnel of LSTM-Erlangen.

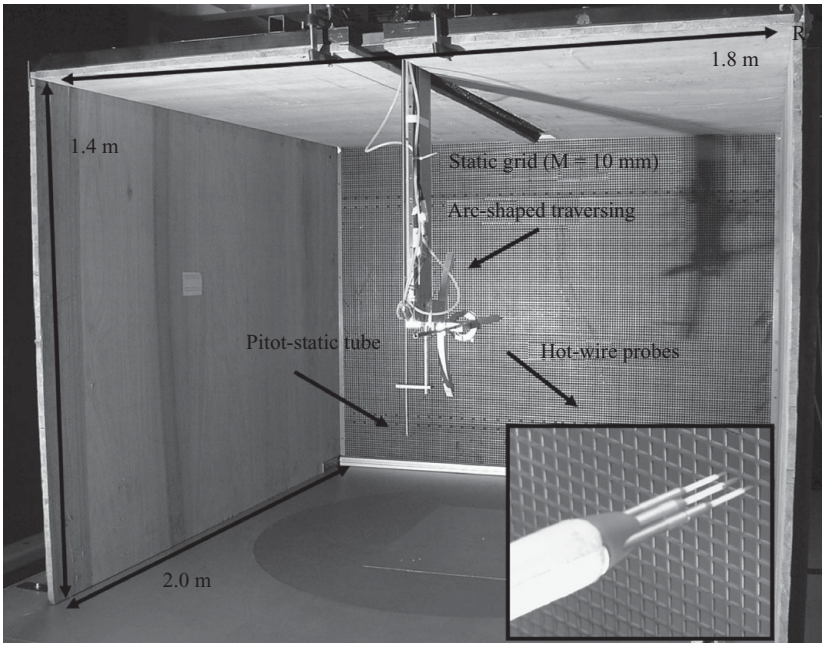

FIGURE 2. The test section of the wind tunnel and the installed measurement system.

In figure 2, the test section, the static-grid structure, the hot-wire probe and other measurement equipment employed are shown. The ratio of any one of the cross-sectional dimensions of the test section to the mesh size was much larger than 1.

A square punched grid structure with a 10 mm mesh size, M, with 64 % porosity was installed at the exit of the contraction. The standard deviation of the bar width of the grid structure was measured to be 2.4 %, which corresponds to a 1.3 % standard deviation of the porosities of cells of the grid structure. In accordance with the above-mentioned studies, the mesh size is defined as the distance from the centre of one rod to the next. The selected mesh size allowed measurements to be conducted at distances more than 100 M downstream of the grid in this test section. The grid Reynolds number,

$$Re_M = \frac{U_m M}{\nu}, \tag{2.1}$$

was controlled by setting the mean flow speed in the test section, U_m. In this way, the effects of grid Reynolds number on the inhomogeneity of measured turbulence quantities could be checked. The turbulence Reynolds number based on Taylor length scale and longitudinal velocity fluctuation $\left(Re_\lambda = \sqrt{\overline{u_1 u_1}}\lambda_g \nu\right)$ remained below 100. Hence, according to Mydlarski & Warhaft (1996), generated turbulence can be accepted as weak turbulence (the turbulence is called strong for $Re_\lambda \geqslant 200$). Re_λ drops in the flow direction. The range of Re_λ for each flow case is given in table 1. The details of scale and corresponding Re_λ development in the experiments were documented by Ertunç (2007).

The wind tunnel was equipped with temperature control, which kept the flow at a given temperature within ± 0.5 K. The maximum operating speed in the test section could be set up to 60 m s^{-1}. Because of the large drag force applied on the grid at high velocities and the resulting deformation of the grid, only velocities up to 12 m s^{-1} were used.

To conduct velocity measurements, a DISA 56C01 hot-wire anemometer unit with four DISA CT56C17 constant-temperature hot-wire bridges was employed. Two single normal wire (SN-wire) and one X-wire probes were used. The probes were mounted on an arc-shaped traversing system enabling the angle between the probe and the flow to be varied between 25° and −25° in 5° steps. This system was used to perform angle calibration of the X-wire probe. As can be seen in figure 2, the arc-shaped traversing together with hot-wire probes were installed on a three-dimensional traversing system. This probe configuration was selected to account for the irrotational velocity fluctuations appearing as flow disturbances. They become visible when the turbulence level drops below 0.1 %. Since these kinds of fluctuations are global in nature, i.e. they happen to occur in the whole test section, cross-correlation of two SN-wires separated sufficiently from each other is a measure of those fluctuations. Knowing the irrotational fluctuations, $\overline{u_1 u_1}$ values were corrected simply by subtracting the irrotational contribution. The theoretical background of the design of this probe system and the necessary measurement and data processing methods were given in detail by Ertunç (2007) and Ertunç & Durst (2008). As the above-mentioned flow rate fluctuations occur simultaneously everywhere, no influence on the homogeneity of the turbulence field was observed.

The normal wires were 0.8 and 1.0 mm in length and the two inclined wires of the X-wire probe were 1.2 mm in length. The distance between the inclined wires of the X-wire probe was 1.0 mm and their geometric inclinations were 43° and 44° with respect to the probe axis. All the hot wires employed were 5 μm in diameter. In order to minimize the electronic noise, the gain and high-frequency filter settings of the hot-wire bridge amplifier were chosen to be 1. With these settings, the anemometer had a cut-off frequency of 22 kHz at a flow speed of 12 m s^{-1}. The signals from the

anemometers were filtered through low-pass filters integrated in the back-up amplifiers with their upper frequency limit set at 11 kHz. This upper frequency limit was much higher than the expected highest frequencies of the turbulent velocity fluctuations. The highest frequency was estimated from order of magnitude considerations to be 8 kHz at the maximum.

The calibration of the hot wires in the wind tunnel was performed with the reference velocity obtained from a Pitot-static tube installed on the traversing system in the vicinity of the hot-wire probes. A Setra differential pressure transducer was employed for the measurements with the Pitot-static tube. During the calibration and measurements, the temperature of the flow was measured with a PT100 temperature sensor in order to correct the measured data for temperature drift. For the angle calibration of the X-wire probe, the effective angle method suggested by Bradshaw (1971) was applied. As at the same location the longitudinal velocity was measured with the Pitot-static tube, we checked the accuracy of the calibration with the longitudinal velocity component. The transverse component was essentially zero. During the measurements, no substantial deviation of the streamwise velocity measured by the hot-wire probes from that measured by the Pitot-static tube was observed.

The filtered hot-wire signals and the pressure transducer and temperature signals were acquired via a 16-bit A/D converter (NI 6052E DAQ card) installed in a personal computer. The data were stored on hard disks for post-processing. All the signals were grounded only over the computer in order to prevent ground loop disturbances on the measured signal. During the measurements, a resolution of 0.076 mV was achieved with the A/D converter. The minimum r.m.s. voltage reading of an analog r.m.s. meter with turbulence-free flow was around 0.2 mV. Hence, the resolution of the data acquisition system permitted low-turbulence intensity measurements with high digitalization accuracy.

The sampling rate for each set of measurements, except when the spectra and the two-point correlation functions were measured, was chosen such that only statistically uncorrelated data were sampled. For this purpose, the integral time scales, τ, were estimated via the autocorrelation function of the measured velocity fluctuations. For every measurement case, the sampling frequency was chosen such that they were less than $1/2\tau$ to ensure zero eddy turbulence correlation between two consecutive data. The number of data for each measurement point was 50 000, which resulted in less than 1 % statistical uncertainty with 99 % confidence for the mean velocity and around 1.2 % statistical uncertainty with 95 % confidence for the mean square of the turbulent velocity fluctuations.

The hot-wire measurements comprise scans of a plane, which is perpendicular to the grid, located about the centre of the test section and extends 1060 mm in the streamwise direction and 50 mm in the transverse direction. The transverse resolution of the scan was 1 mm. Since such a measurement field corresponds to a long narrow strip, the measured field could only be visualized by reducing the aspect ratio in the plots.

2.2. *Analyzed quantities*

The scanned planes consist of N_{x_1} points in the flow direction and N_{x_2} points in the transverse direction, such that the spatial resolutions of the scan in the two directions are Δx_1 and Δx_2.

In order to visualize the homogeneity of any one of the measured or simulated mean quantities, say $\overline{H}$, in the scanned plane, the inhomogeneity parameter $I_{\overline{H}}$ at

$x_1 = i\Delta x_1$ and $x_2 = j\Delta x_2$ is defined as

$$I_{\overline{H}}(x_1, x_2) = \left[\frac{\overline{H}(i\Delta x_1, j\Delta x_2) - \dfrac{1}{N_{x_2}} \displaystyle\sum_{k=1}^{N_{x_2}} \overline{H}(i\Delta x_1, k\Delta x_2)}{\left| \dfrac{1}{N_{x_2}} \displaystyle\sum_{k=1}^{N_{x_2}} \overline{H}(i\Delta x_1, k\Delta x_2) \right|} \right] \times 100, \tag{2.2}$$

which is the percentage deviation of the variable $\overline{H}(x_1, x_2)$ from the absolute value of its average value calculated along a line having $x_1 = \text{constant}$. The inhomogeneities of the mean longitudinal velocity $I_{\overline{U}_1}$ and the Reynolds stresses $I_{\overline{u_1u_1}}$ and $I_{\overline{u_2u_2}}$ are analysed in the following in more detail. Anisotropies of Reynolds stresses, which are non-dimensional parameters, are of vital importance for modelling and predictions. Therefore, the field of stress anisotropy and its inhomogeneity is visualized by using the anisotropy of the longitudinal normal Reynolds stress a_{11}, which is

$$a_{11} = \frac{\overline{u_1u_1}}{q^2} - \frac{1}{3}, \tag{2.3}$$

where $q^2 = \overline{u_1u_1} + \overline{u_2u_2} + \overline{u_3u_3}$ and can be approximated by $q^2 \approx \overline{u_1u_1} + 2\overline{u_2u_2}$ in nearly homogeneous and axisymmetric turbulence, which should be the case when turbulence is generated with uniform and symmetric grids in all transverse directions.

In an ideal homogeneous turbulence, distribution functions of any velocity fluctuation f, for instance streamwise and transverse velocity fluctuations, should show a symmetry around their zero mean and should have a normal distribution. The symmetry is monitored through the skewness factor

$$S_f = \overline{f^3}/f'^3. \tag{2.4}$$

For a perfect symmetric distribution, the skewness factor should be zero. The flatness factor,

$$F_f = \overline{f^4}/f'^4, \tag{2.5}$$

is a measure of the normal distribution and it should be 3 for a perfect normal distribution. Within the analysis of each case, fields of the skewness and flatness factors of velocity fluctuations S_{u_1}, S_{u_2}, F_{u_1} and F_{u_2} are presented.

2.3. *Experimental results*

The inhomogeneity of the mean velocity field at mesh Reynolds number $(Re_M) = 8000$ is shown in figure 3. The red colour indicates regions of higher velocity and the blue colour indicates regions of lower mean velocity than the mean of the mean velocity along a line having $x_1 = \text{constant}$. The locations of grid rods are depicted as black bars on the vertical axis. It is obvious that the mean velocity decreases behind the rods and increases in the open area between two rods. In the vicinity of the grid $x_1/M < 10$, inhomogeneity of the streamwise velocity is over $\pm 10\,\%$, but it decreases to below $\pm 2\,\%$ for $x_1/M > 15$. $I_{\overline{U}_1}$ levels to $\pm 1\,\%$ for $x_1/M > 50$. The inhomogeneity of the normal stress $\overline{u_1u_1}$ for different flow speeds, i.e. $Re_M = 4000, 5333$ and 8000, are shown in figure 4. Broadly seen are the regions having either positive or negative deviations extending in the whole streamwise directions. These regions repeat in a cyclic manner in the transverse direction, but not with a periodicity of mesh size M. The total measuring time of one of these planes for one Re_{M} was around three days. Hence, it is really impressive to observe the standing regions of inhomogeneity behind

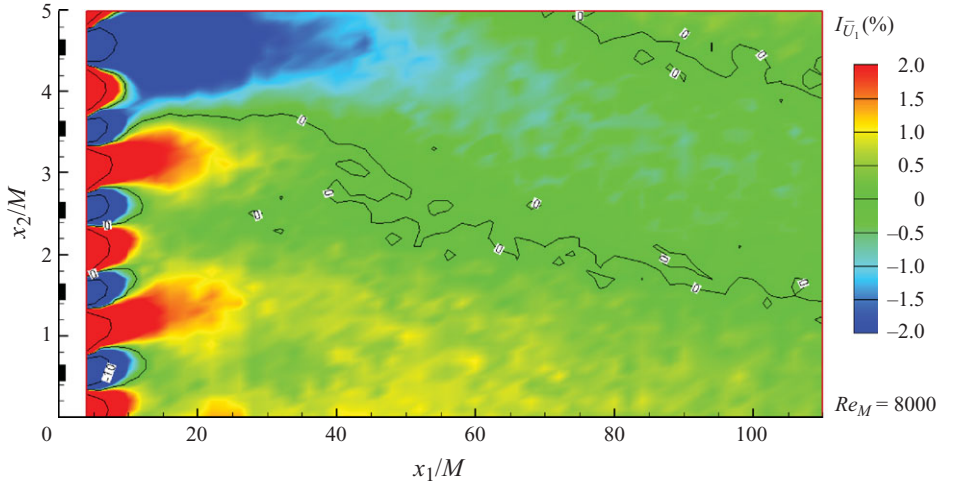

FIGURE 3. Inhomogeneity of mean velocity field $\overline{U}_1(x, y)$ at the wake of the grid in the wind tunnel having a porosity of 64 % at $Re_M = 8000$.

the grid even after 100 mesh sizes and the persistence of these regions almost at the same locations for all Reynolds numbers.

The inhomogeneity of $\overline{u_2 u_2}$ at $Re_M = 8000$ is shown in figure 5. In the inhomogeneity fields of stresses, traces of each grid rod can clearly be seen up to $x_1/M \approx 12$. These regions correspond to the separated wake flow of the rods. Inhomogeneity of velocity fluctuations behind the rods is positive for $Re_M = 5333$ and 8000, whereas at the same positions inhomogeneity of the mean velocity field takes negative values. In figures 4 and 5, positive regions coalesce with positive regions and vice versa for $x_1/M > 10$, so that wider strips of positive and negative regions occur, which further coalesce with each other downstream of the grid. In three dimensions, the inhomogeneity field can be imagined as being composed of continuously braiding positive and negative strips. Downstream of the grid, the levels of inhomogeneities of the normal stresses do not drop and fluctuate spatially between ± 5 % and the inhomogeneity level of off-diagonal stress fluctuates between ± 50 %. It can be concluded that measurements of normal stresses along any two lines with $x_2 =$ constant might deviate by ± 5 % from each other.

The anisotropy a_{11} field and its inhomogeneity $I_{a_{11}}$ field are shown in figure 6. In the flow direction, a_{11} has a tendency to drop (figure 6*a*). However, a_{11} decreases faster close to the grid, and further downstream it levels to some value, which is dependent on the grid Reynolds number and the measurement location. In the paper by Comte-Bellot & Corrsin (1966), a_{11} took a maximum value of 0.143 and a minimum value of 0.02 at $x_1/M \cong 20$. In our experiments, the approximate values of a_{11} are 0.12 and 0.06, respectively, at the corresponding locations. Considering that these values are dependent on the grid-type as shown by Comte-Bellot & Corrsin (1966) and also dependent on the transverse location of the measurement probe as shown in figure 6, the present data are within the range found in the literature. Ertunç (2007) showed that regions with higher values of a_{11} in the vicinity of the grid become larger with increase in grid Reynolds number. The inhomogeneity of a_{11} also becomes stronger close to the grid and the negative and positive strips of inhomogeneity can also be seen in figure 6(*b*) with deviations approaching ± 20 % far downstream of the grid.

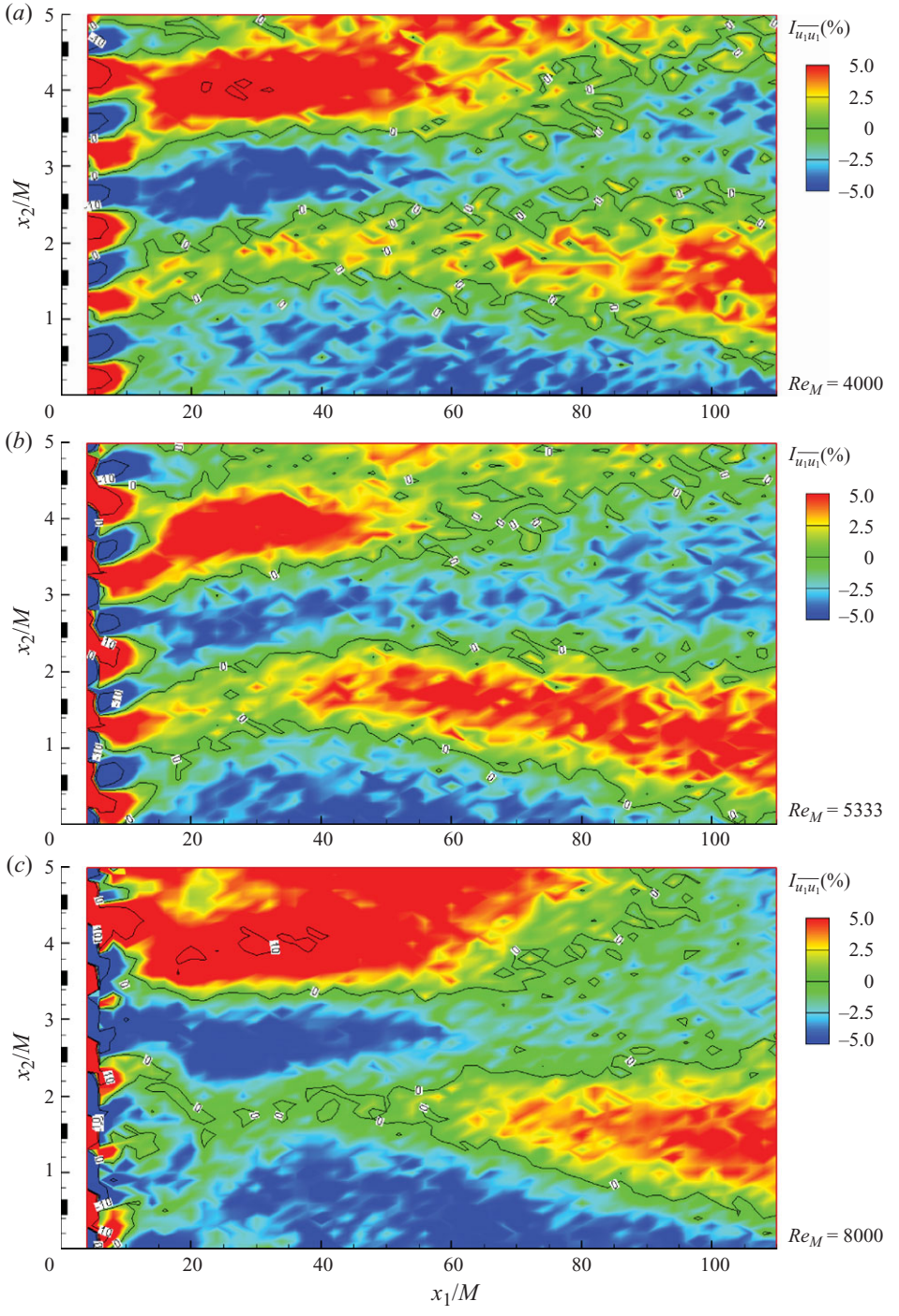

FIGURE 4. Inhomogeneity of $\overline{u_1u_1}(x, y)$ field at the wake of the grid in the wind tunnel having a porosity of 64 % for different grid velocities at (*a*) $Re_M = 4000$, (*b*) 5333 and (*c*) 8000.

The skewness and flatness factors of u_1 fluctuations and, particularly, u_2 fluctuations also show spatially inhomogeneous fields. Examples of these fields of u_2 fluctuations are presented in figure 7 for $Re_M = 8000$. For $x_1/M > 12$, the skewness factors take

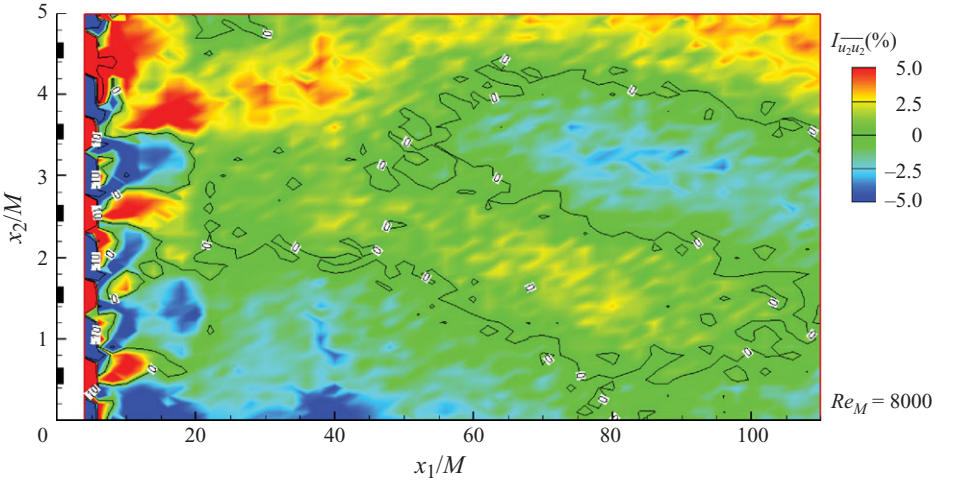

FIGURE 5. Inhomogeneity of $\overline{u_2u_2}$ field at the wake of the grid in the wind tunnel having a porosity of 64 % at $Re_M = 8000$.

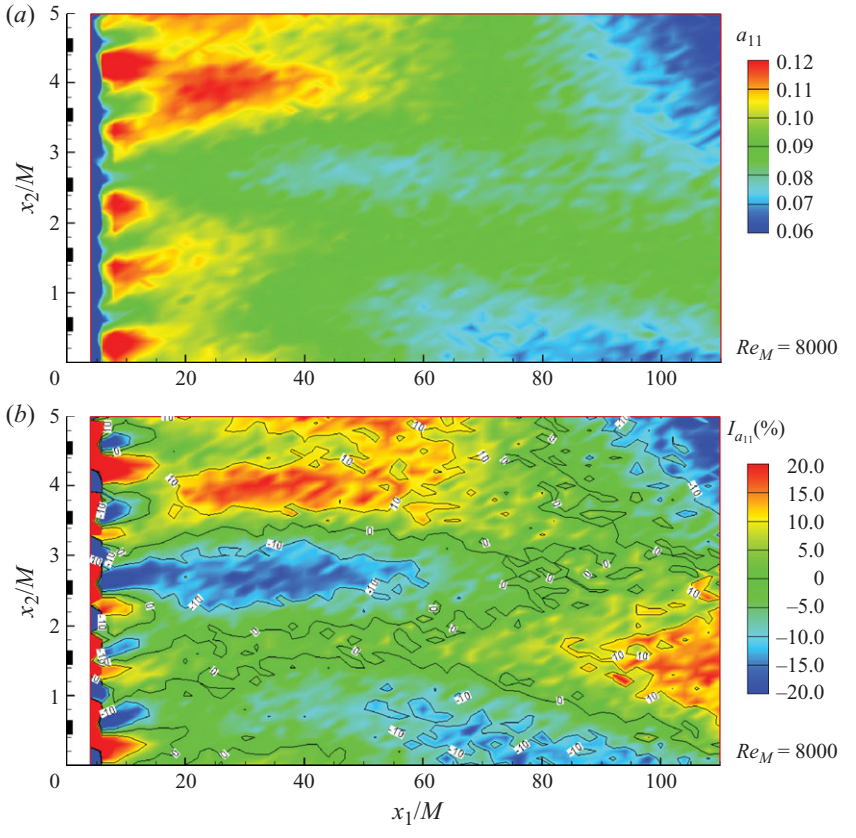

FIGURE 6. (*a*) a_{11} field and (*b*) its field of inhomogeneity at the wake of the grid in the wind tunnel having a porosity of 64 % at $Re_M = 8000$.

values ± 0.1. In the detailed analysis of the measured data, Ertunç (2007) showed that the spatial inhomogeneity of F_{u_2} close to the grid grows with increase in Reynolds number. Further downstream of the grid, both flatness factors, F_{u_1} and F_{u_2}, have a

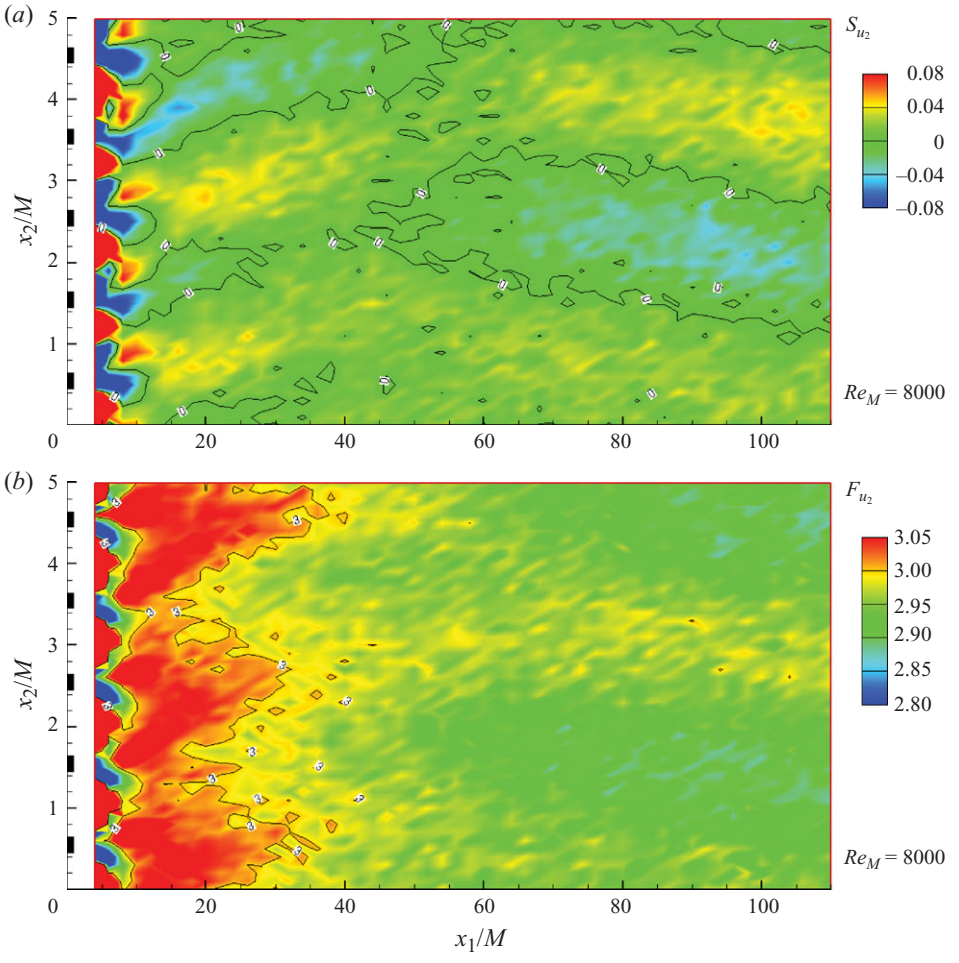

FIGURE 7. (*a*) Skewness factor $S_{u_2} = \overline{u_2^3}/u'^3_2$ and (*b*) flatness factor $F_{u_2} = \overline{u_2^4}/u'^4_2$ of u_2 fluctuations at the wake of the grid in the wind tunnel having a porosity of 64 % at $Re_M = 8000$.

tendency to be less than three and take values between 2.85 and 3.0. This shows that large-amplitude fluctuations are less probable than expected for a normal distribution. Nevertheless, when only the symmetry of the velocity fluctuation distribution and its form are considered to be the criteria of homogeneity, measured skewness and flatness values downstream of the grid give an impression that the flow field is homogeneous, although there exists a spatial inhomogeneity of the measured mean quantities.

All the evaluated fields in the selected very small portion of the flow do not possess full symmetry downstream of the grid structure in the transverse direction. The turbulence is generated as a result of the highly unsteady outgoing jets. The coalescence of these jets has an unstable nature, as was discussed earlier, and only after averaging did the most probable locations of the coalescence become visible. The resulting asymmetry in the inhomogeneity fields can be contributed to by the slight non-uniformity (1.3 % in its porosity) of the grid structure. Owing to the random distribution of this non-uniformity over the whole grid structure, similar asymmetry should be expected in other downstream planes. Whether the observed inhomogeneity is solely due to the non-uniform grid structure will be elucidated with the help of DNS in § 3.

3. Numerical investigations

For the DNS investigations, the standard LBGK was employed. The main goals of the simulations were, above all, to see whether the experimentally observed inhomogeneities could be confirmed and to see whether the porosity of the grids has an influence on the inhomogeneity. For this purpose, four porosities, 53 %, 64 %, 72 % and 82 %, were studied at a fixed mesh Reynolds number, $Re_M \approx 1400$ (table 1). Furthermore, the effect of non-uniformity in the geometry of the grid structure was investigated to determine whether the inhomogeneities observed in experiments are caused by slight non-uniformities of grid structures.

In order to determine the effect of the size of the computational domain, an extra simulation was conducted with an approximately six times larger domain for the 72 % porosity grid.

3.1. *The numerical method*

The origin of the Lattice Boltzmann equation (LBE), more specifically the Boltzmann equation, is based on the kinetic theory, and it describes basically the evolution of the velocity distribution function on a lattice in such a way that the macroscopic fluid dynamics behaviour (Navier–Stokes equations) can be recovered by applying the Chapman-Enskog expansion. In the absence of external forces, the general LBE reads

$$f_\alpha(x + \xi_\alpha \delta_t, t + \delta_t) = f_\alpha(x, t) + \Omega_\alpha(f), \tag{3.1}$$

where f_α denotes the single-particle distributions, ξ is the microscopic velocity, α is the direction of these discrete velocities and Ω is the collision integral. The macroscopic quantities (density and velocity) are then given by

$$\left.\begin{aligned} \rho &= \sum_\alpha f_\alpha, \\ \rho \boldsymbol{u} &= \sum_\alpha \xi_\alpha f_\alpha. \end{aligned}\right\} \tag{3.2}$$

At each time step, the velocity distribution functions at each point are re-evaluated based on three main processes: collision, propagation and bounce-back. The collision operator, Ω, can be linearized either by using single-time relaxation or by multiple relaxation parameters. Depending on this, two different methods of Lattice Boltzmann calculations exist: single-time LBE (BGK) and multiple relaxation methods (MRT) (see, for example, Wolf-Gladrow 2000; Succi 2001). The former method was employed in the present study.

3.2. *Computer code employed and computational details*

For the computations in the present study, we employed a Lattice Boltzmann BGK solver, known as the BEST code, which was developed at LSTM Erlangen. It was parallelized by MPI standard and optimized for various cache- and vector-based platforms, including the NEC-Sx8 series (Stuttgart HPC centre) and HLRB II (Leibnitz HPC centre), where the presented calculations were carried out. This code has been verified by various researchers for many different applications, ranging from the investigations on plane channel flows at low-to-moderate Reynolds numbers (Özyılmaz 2003; Lammers 2004) to the investigation of flows through complex geometries, such as porous media and fixed-bed reactors (Zeiser *et al.* 2001; Freund *et al.* 2003). In many studies, it was shown to be at least as accurate as and more efficient than the traditional CFD methods (Breuer *et al.* 2000; Brenner *et al.*

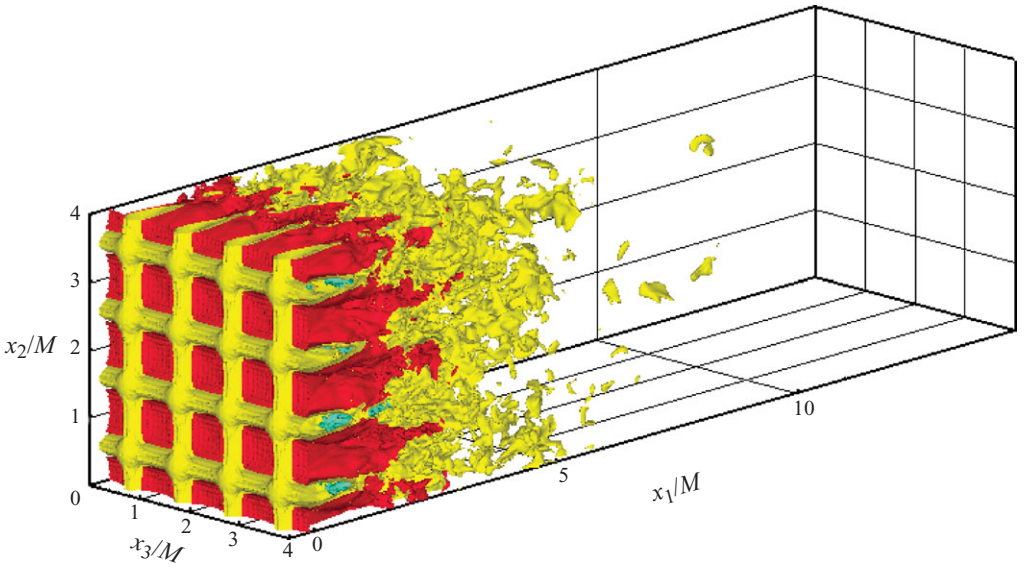

FIGURE 8. A view of the grid in the computational domain and the instantaneous streamwise velocity field for the flow case with 53 % porosity.

2003; Wellein *et al.* 2006). Hence, it was an ideal candidate for further clarifications regarding the (in)homogeneity of the turbulent quantities of grid-generated turbulence at intermediate Reynolds numbers by DNS.

As mentioned previously, we conducted DNS for four different porosities, using square rods. By keeping the mesh size the same ($M = 40$), the thickness of the rods was changed to obtain the desired porosity. The applied obstacle can be inferred from figure 8, where the instantaneous streamwise velocity component is visualized. The mesh Reynolds number was fixed at $Re_M \approx 1400$. The flow was driven by a constant pressure drop in the main flow direction. We applied periodic boundaries as inlet/outlet boundary conditions, combining them with the 'fringe region method'. The latter was used to justify the application of periodic boundaries in the non-periodic streamwise direction, as suggested first by Spalart (1988). The present simulations were conducted based on the knowledge that the total number of points required for a DNS in isotropic turbulence is proportional to $Re_L^{11/4}$, if one would like to resolve the smallest scales both in space and in time (Breuer 2001). Considering this relation, around 2.88×10^6 points were required, for instance, to carry out simulations at $Re_\lambda \approx 25$. Taking into account that the lateral extent ($L_{x_2} = L_{x_3}$) of the computational domain must be larger than the length of the energy-containing eddies, which is of the same order as the mesh size, M, in grid-generated turbulence, the final grid resolution was chosen to be $2400 \times 160 \times 160 = 6.144 \times 10^6$, i.e. $L_{x_2}/M = 4$. As discussed below, we checked the influence of the L_{x_2}/M ratio on the inhomogeneity of the mean velocity component, using $L_{x_2}/M = 10$. This study resulted in no significant differences, hence we applied the lower grid resolution for the study. Another way to check the quality of the grid resolution is to examine the Kolmogorov length scale obtained from the simulations. In figure 9, the ratio between the spatial resolution of the grid (Δ) and the Kolmogorov length scale (l_k) is provided. When interpreting these results, one should keep in mind that the Kolmogorov length scale was derived based on an order-of-magnitude consideration, hence, to describe the spatial resolution of the

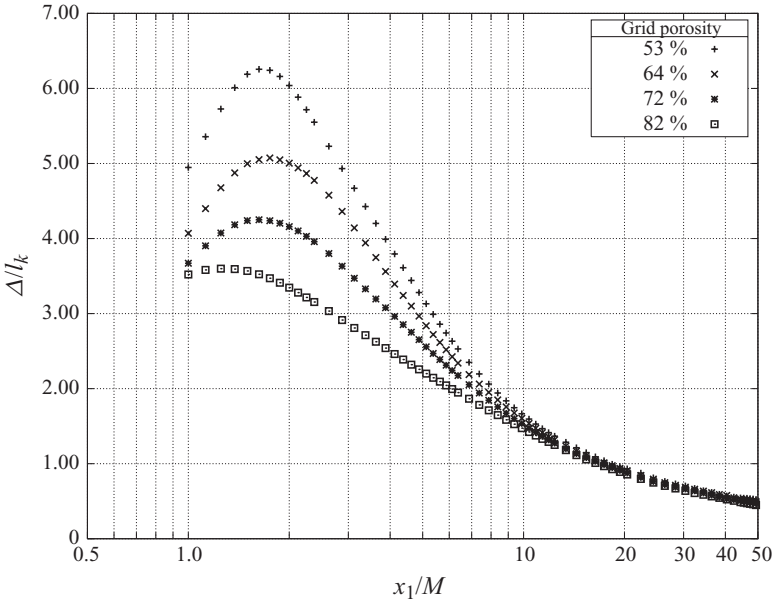

FIGURE 9. Development of the ratio between the spatial resolution of the grid (Δ) and the Kolmogorov length scale (l_k) in the streamwise direction for different porosities.

smallest scale a prefactor higher than one might be needed (Fröhlich 2006). As seen in figure 9, in many of the investigated cases Δ/l_k is less than five for the whole streamwise extent and less than one for $x_1/M > 20$. Therefore, the spatial resolution of the present simulations was accepted as adequate enough for the current purposes. It should be noted that in a previous Lattice Boltzmann simulation by Djenidi (2006), a much lower grid resolution was employed for $Re_M = 1600$.

3.3. *Numerical results*

The time averaging of the turbulent quantities to be discussed in this section was carried out as follows: once the turbulence field was developed, the mean velocity statistics were accumulated. After obtaining approximately 15 000 (t_{final}) independent samples for the mean velocity components, samples for Reynolds stress components were started to be collected, using the mean velocity fields corresponding to (t_{final}). We carried on the sampling until we had around 15 000 independent samples for the Reynolds stresses as well. An intermediate post-processing was carried out after 10 000 ($t_{intermediate}$) samples. In relation to this work, no important difference was observed between the statistics of the ($t_{intermediate}$) and (t_{final}). On the other hand, the results shown in the following correspond to (t_{final}).

In order to study the effect of porosity on the (in)homogeneity of mean velocity and Reynolds stress components, we chose a fixed position in the spanwise direction and calculated the inhomogeneity values according to (2.2). The results shown in the following correspond to the spanwise position which lies in the middle of the computational domain. We also carried out the same processing at different spanwise positions. Since the qualitative observation was always the same, only one set of the results is presented in the following.

Figure 10 shows the inhomogeneities of the time-averaged mean velocity component for different porosities. The inhomogeneity level for $x_1/M > 20$ corresponds approximately to those of the experiments discussed in the preceding section, which

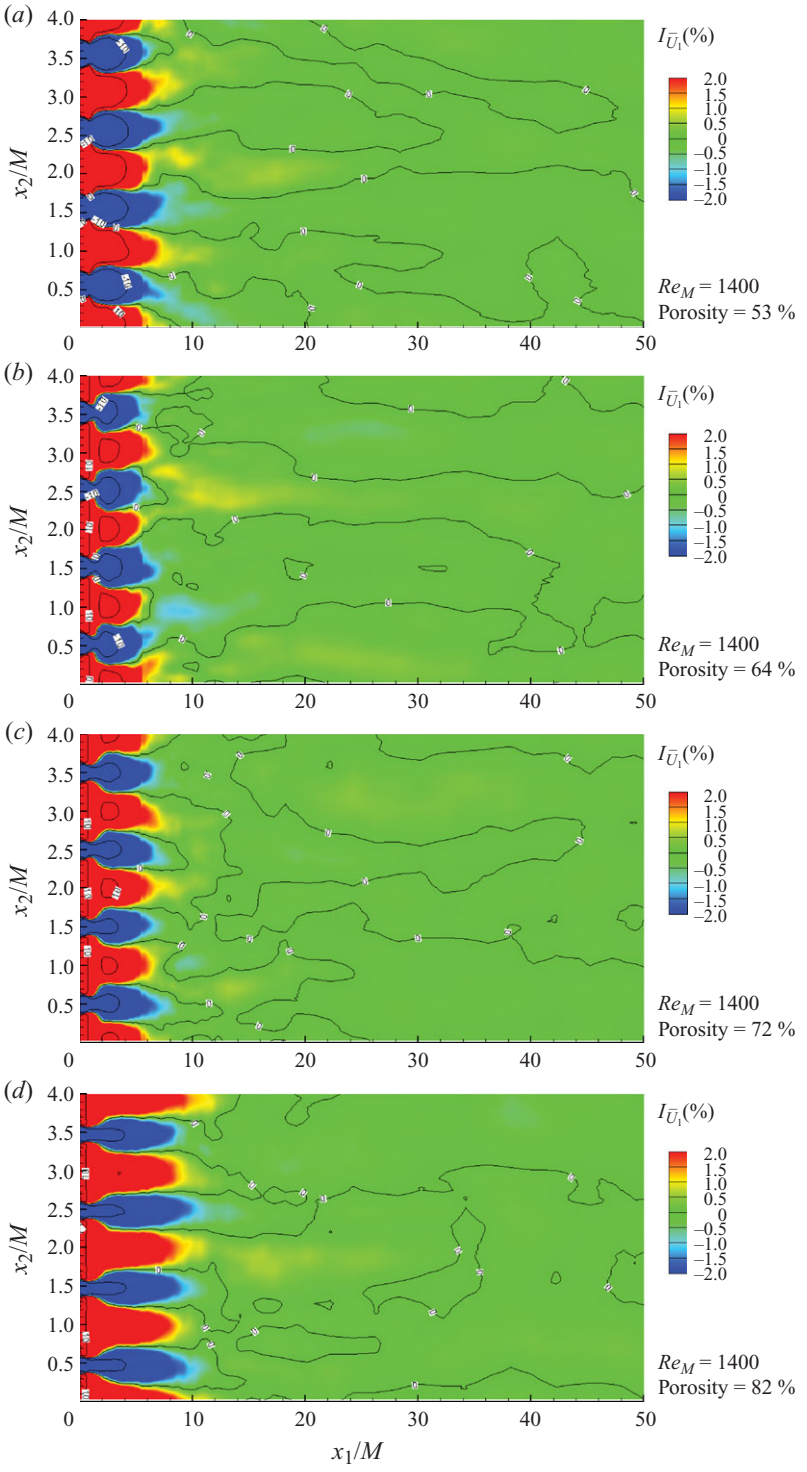

FIGURE 10. Inhomogeneity of mean velocity $\overline{U}_1$ for different porosities: (*a*) 53 %, (*b*) 64 %, (*c*) 72 % and (*d*) 82 %.

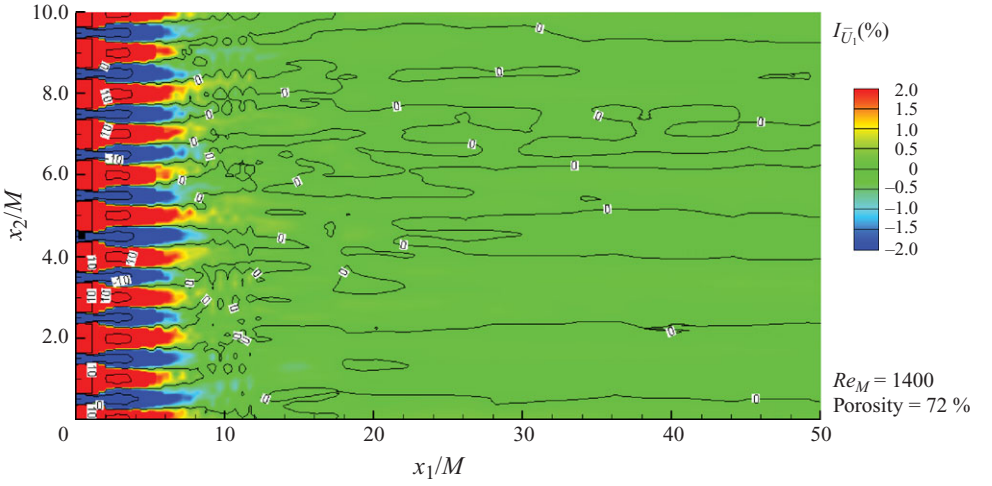

FIGURE 11. Inhomogeneity of mean velocity $\overline{U}_1$ for 72 % porosity with grid resolution $2400 \times 400 \times 400$.

are ± 2 %. In the vicinity of the grid ($x_1/M < 10$), higher inhomogeneity is observed. Far from the grid, no trace of inhomogeneity is left. Obviously, the mean velocity component is homogeneous. This conclusion is in agreement with Corrsin (1963) in the sense that the streamwise mean velocity is homogeneous; however, no dependence on the porosity of the grid can be inferred from these data; even for a porosity value as low as 53 % the mean velocity field stays homogeneous. However, as discussed in the previous section, although not too high, the measurements revealed some regions of inhomogeneous mean velocity fields (figure 3). This difference between the experimental and computational results is yet to be clarified.

In the computations, we employed four rods in each direction in the computational domain. In order to see if the number of the rods has any effect on the (in)homogenization of the mean velocity, we extended the computational domain in the transverse and spanwise directions by a factor of 2.5. In other words, we kept the thickness of the rods and the mesh size the same, but instead of using four rods, we introduced 10 rods to the domain and repeated one of the previous calculations (72 %) with a resolution of $2400 \times 400 \times 400$. The outcome of this extra simulation is presented in figure 11. As can be clearly seen, the size of the computational domain has no influence on the level of inhomogeneity of the mean velocity. As in the previous computations, only near the grid (for $x_1/M < 10$) are small inhomogeneities observable.

There is another factor, however, which might have caused the difference between the experiments and numerical results in terms of the inhomogeneity of the mean velocity: a probable difference in the geometry of the grid used in both studies. The grid used in the numerical simulations was perfectly uniform in all directions. On the other hand, there might be some manufacturing imperfections in the grids employed in the experiments. It was possible to remove this factor by another DNS, where we used slightly modified rods. Since the extension of the transverse and spanwise directions of the computational domain did not show any important influence, we conducted this computation again with a resolution of $2400 \times 160 \times 160$ for a porosity of 72 %. The two rods in the upper half of the computational domain were kept exactly the same as the rods employed in the previous runs. The dimensions of the

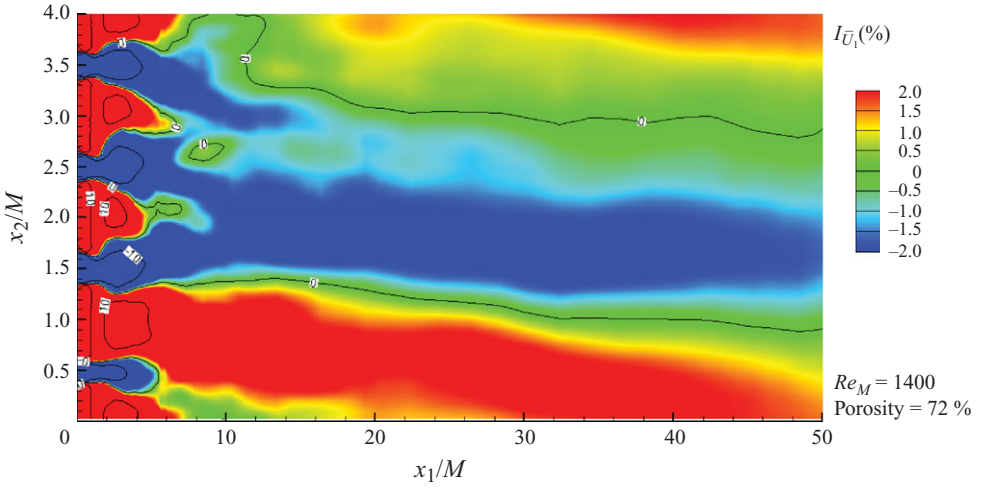

FIGURE 12. Inhomogeneity of mean velocity $\overline{U}_1$ for 72 % porosity with non-uniform grid.

lower rods were modified in order to introduce non-uniformity to the geometry. By increasing the number of points by one in both the vertical and spanwise directions, the lowest rod became wider in these two directions. Similarly, by decreasing the number of points by one, both in vertical and spanwise directions, the other rod became narrower in these two directions. The grid was positioned in the streamwise direction in the same location as before. The symmetric rods had a thickness of 6 in lattice units. Hence, modification of its width by one leads to a difference of around 17 % in each direction. At first glance this modification might seem to be unrealistically high. However, the main aim of this simulation was not to be able to reproduce the results observed in the experiments but to be able to show the trend eventually caused by possibly non-uniform geometries. The outcome of this simulation is shown in figure 12. The part of the field aligned with the modified rods became greatly inhomogeneous. This study showed very clearly that the mean velocity tends to be inhomogeneous far downstream of the grid, if non-uniform grid structures are employed.

The discussion up to now allows us to draw the fair conclusion that the streamwise mean velocity component is homogeneous in grid-generated turbulence, even for a Reynolds number as low as $Re_M \approx 1400$, provided that one is sure about using perfectly uniform geometries. Regardless of the value of the porosity, the mean velocity is homogeneous; it is homogeneous even for a porosity as low as 53 %.

Of paramount importance in the experiments discussed in the previous section, however, was the highly inhomogeneous fields of 'Reynolds stress' components and their anisotropies. In order to see whether the numerical results are in agreement with those of the experiments, the inhomogeneity of time-averaged Reynolds stress tensor components was calculated. The inhomogeneity of $\overline{u_1u_1}$ for all porosities is presented in figure 13 and the inhomogeneity fields of $\overline{u_2u_2}$ and a_{11} are shown in figures 14(a) and 14(b), respectively, only for a 64 % porous grid. Obviously, the Reynolds stress tensor is tremendously inhomogeneous. The degree of inhomogeneity is of comparable order for $\overline{u_1u_1}$ and $\overline{u_2u_2}$ with the higher levels observed in the experiments. The anisotropy of the Reynolds stress tensor (a_{11}) shows ± 20 % inhomogeneity (figure 14b), which is comparable to those of the experiments (figure 6b).

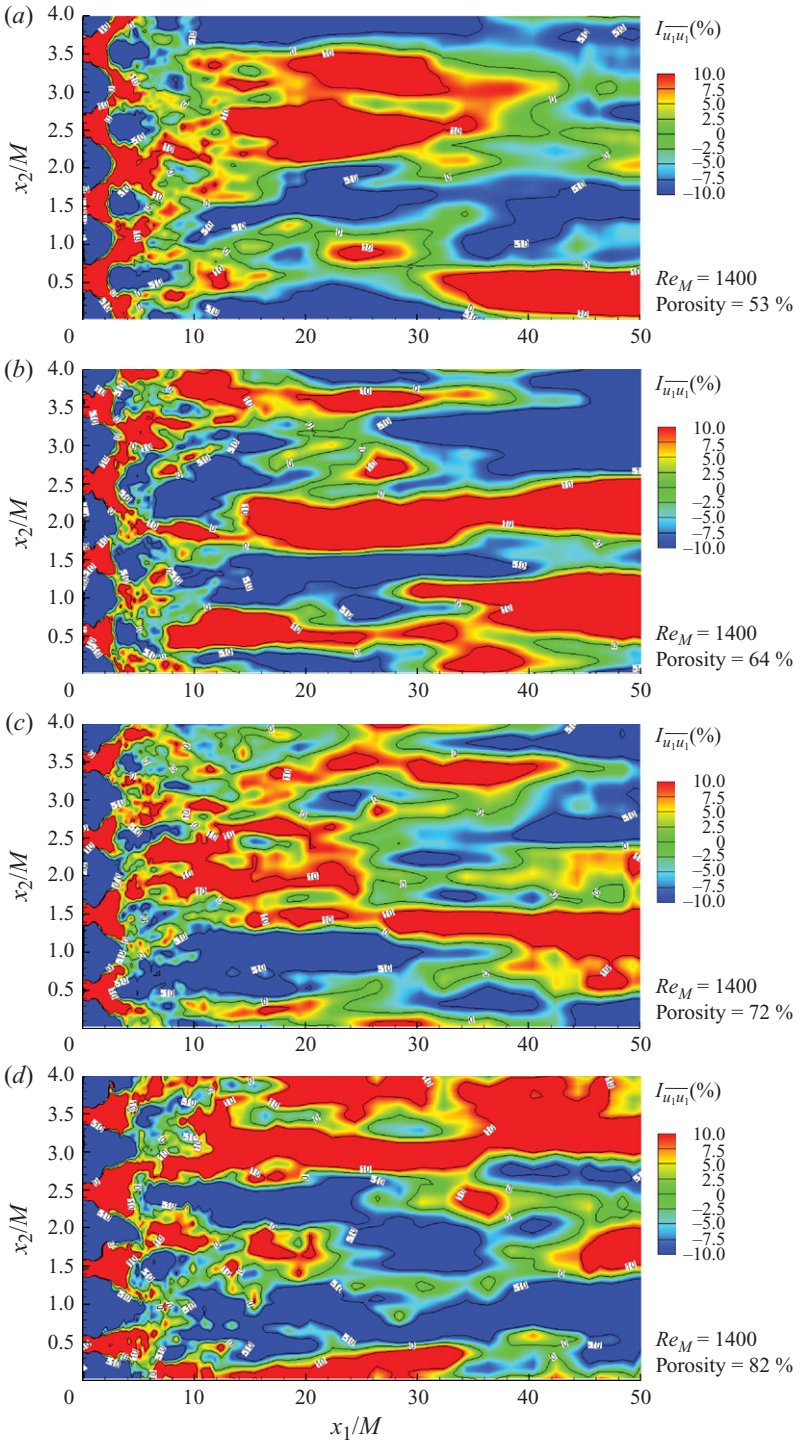

FIGURE 13. Inhomogeneity of $\overline{u_1u_1}$ for different porosities: (*a*) 53 %, (*b*) 64 %, (*c*) 72 % and (*d*) 82 %.

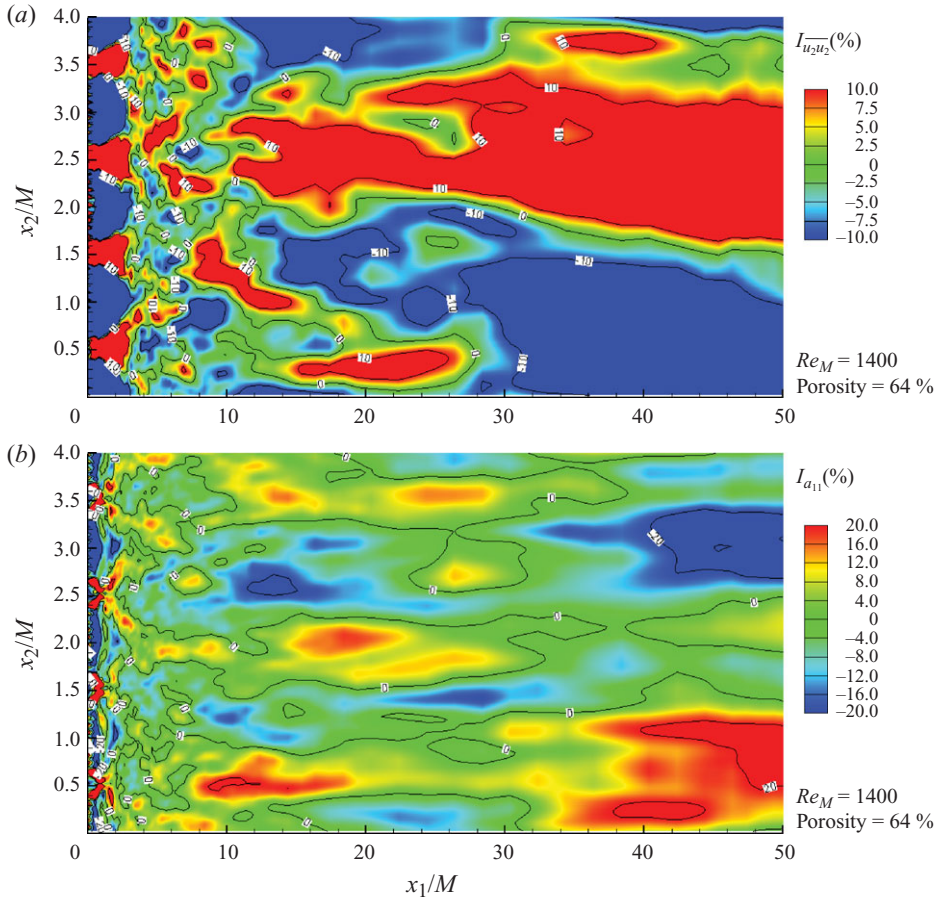

FIGURE 14. Inhomogeneity of (*a*) $\overline{u_2u_2}$ and (*b*) a_{11} for 64 % porosity.

Although there may be quantitative deviations from the experimental study presented above, the overall trend is also confirmed by the numerics: Reynolds stress components are strongly inhomogeneous. DNS for different porosities showed that there is no trend towards increasing homogeneity either with increasing x_1/M or with increasing porosity at a fixed mesh size, M.

4. Analysis of the persisting inhomogeneity of Reynolds stresses

The experimental and numerical results of these investigations showed that the symmetric grids produce an inhomogeneous Reynolds stress field but a homogeneous mean velocity field, whereas the simulation with a non-uniform grid structure shows an inhomogeneous mean velocity field in addition to the inhomogeneous stress field. Therefore, we conclude that the inhomogeneity of Reynolds stresses is due to the grid structure itself and the inhomogeneity in the mean velocity field is caused by the non-uniformity of the grid structure. However, the observed inhomogeneity of the mean velocity in experiments and simulations with uniform grid structures had a tendency to decrease, whereas the inhomogeneity of the Reynolds stress field remained independent of the grid structure's uniformity. To explain this, the turbulence kinetic energy field of one of the presented DNS computations is chosen for an analysis to

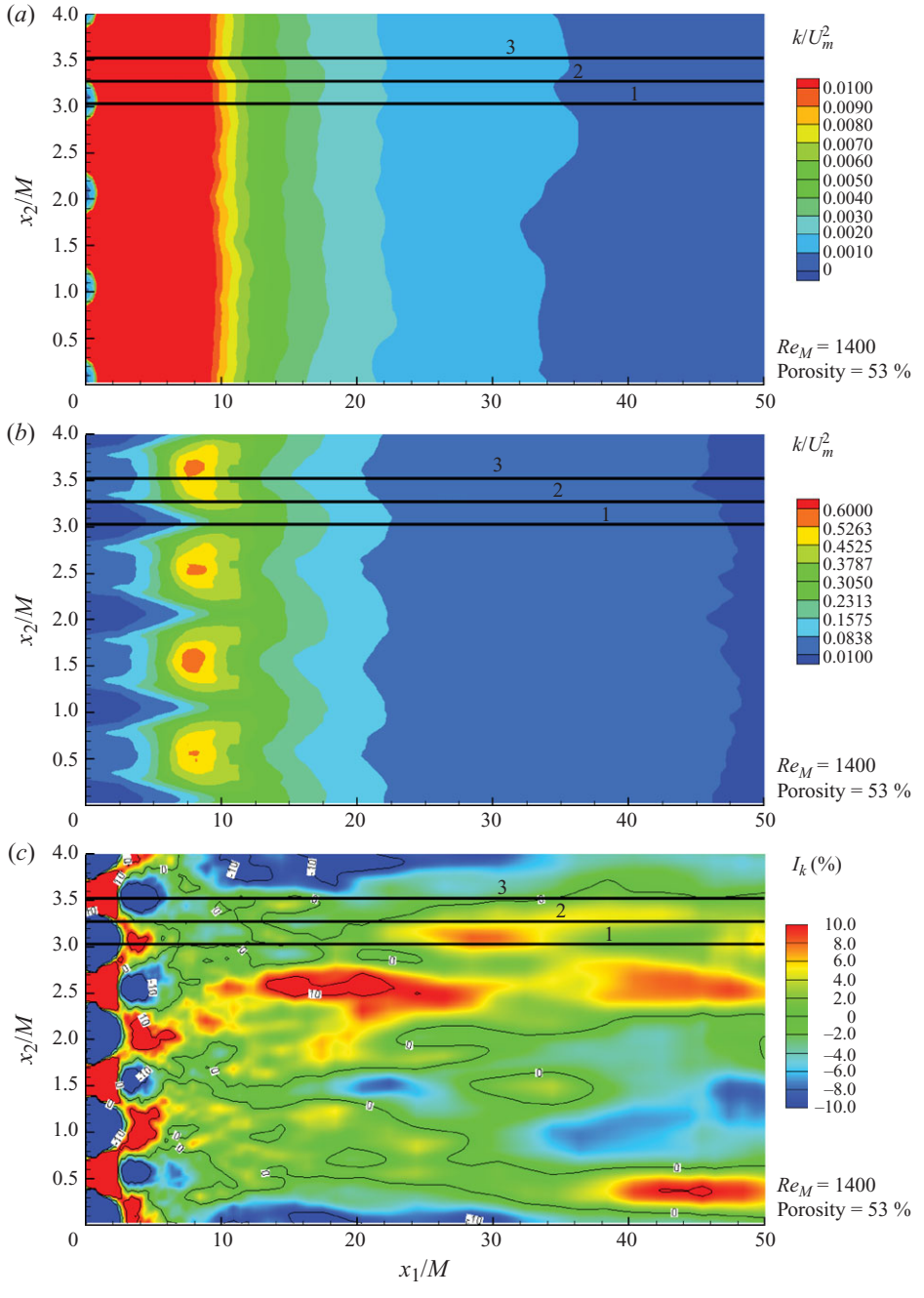

FIGURE 15. (*a*) Kinetic energy field for $0 < x/M < 50$, (*b*) for $x/M < 10$ and (*c*) its inhomogeneity for the simulation made for the grid with 53 % porosity. Kinetic energy field was calculated by Reynolds stress components, which were normalized by the square of the bulk velocity ($U_m = 0.0347$).

understand the persistence of the inhomogeneous Reynolds stress field. The kinetic energy field and its inhomogeneity are shown in figure 15 for the flow case with a 53 % porosity.

The turbulent kinetic energy k is governed by the following averaged equation:

$$\underbrace{\frac{\partial k}{\partial t}+\overline{U}_k\frac{\partial k}{\partial x_k}}_{(I)}=\underbrace{-\overline{u_iu_k}\frac{\partial \overline{U}_i}{\partial x_k}}_{(II)}\underbrace{-\frac{\partial}{\partial x_k}\overline{\left(\frac{p}{\rho}+k\right)u_k}}_{(III)}\underbrace{-\nu\overline{\frac{\partial u_i}{\partial x_k}\frac{\partial u_i}{\partial x_k}}}_{(IV)}+\underbrace{\nu\frac{\partial^2 k}{\partial x_k\partial x_k}}_{(V)}, \tag{4.1}$$

which states that the time derivative of k plus the convective transport of k by the mean motion (I) is equal to the production of turbulence by the mean velocity gradients (II) plus the transport of the total turbulence mechanical energy by turbulent fluctuations (III) plus the major part of the total viscous dissipation of turbulent energy (pseudo-dissipation) (IV) plus the viscous diffusion (V). The time derivative on the left-hand side can be neglected for any ergodic stationary turbulence field under consideration. Thus, according to (4.1), homogenization can be augmented when there is enough turbulence and it is transported by turbulence (III) and viscous diffusion (V). In other words, when mean velocity gradients exist to produce turbulence via term II in (4.1), consequently, terms (III) and (V) become active and homogenization takes place. The contribution of each term to homogenization can be better understood when (4.1) is made non-dimensional for stationary turbulence to read as follows:

$$\begin{aligned}\overline{U}^*_k\frac{\partial k^*}{\partial x^*_k}=&-\overline{u_iu_k}^*\frac{\partial \overline{U}^*_i}{\partial x^*_k}-\left(\frac{q}{\overline{U}_1}\right)\frac{\partial}{\partial x^*_k}\overline{\left(\frac{p^*}{\rho^*}+k^*\right)u^*_k}\\&-\left(\frac{1}{\sqrt{2}Re_L}\right)\left(\frac{q}{\overline{U}_1}\right)\nu^*\overline{\frac{\partial u^*_i}{\partial x^*_k}\frac{\partial u^*_i}{\partial x^*_k}}+\left(\frac{1}{\sqrt{2}Re_L}\right)\left(\frac{q}{\overline{U}_1}\right)\nu^*\frac{\partial^2 k^*}{\partial x^*_k\partial x^*_k},\end{aligned} \tag{4.2}$$

where

$$q^2=2k, \tag{4.3a}$$

$$Re_L=k^{0.5}L/\nu, \tag{4.3b}$$

and L is selected to be the length scale characterizing the large eddies, such that the relation between the turbulence Reynolds number (Re_L) and the Taylor scale Reynolds number (Re_λ) in isotropic turbulence becomes

$$Re_L=\frac{3}{20}Re_\lambda, \tag{4.4}$$

where λ_g is the Taylor's micro scale of turbulence. Hence (4.2) indicates that except the production term, all terms scale with the turbulence intensity ($q/\overline{U}_1$). The dissipation and the diffusion terms are, additionally, inversely proportional to the turbulence Reynolds number (Re_L). Ertunç (2007) showed that Re_λ and, consequently, Re_L decreased downstream of the grid structure despite the increase in λ_g. The turbulence intensity $q/\overline{U}_1$ drops very fast downstream of the static grids, and thereby the contribution of the turbulent transport also drops. Due to the decrease in Re_L, the dissipation and viscous diffusion term is not expected to decrease as fast as the turbulent transport term. Considerations of this kind show that only the dissipation and viscous diffusion terms remain active in the far field of grid-generated turbulent flow. It can also be deduced that only the diffusion term can homogenize the flow before turbulence totally dissipates. It should be noted that in an ideally homogeneous turbulence, the viscous diffusion term is identically zero.

The above considerations can be verified by analysing the turbulence kinetic energy field in figure 15. We select three lines along the flow: line 1 crosses the centre of the open area ($x_2/M=3.05$), line 3 ($x_2/M=3.55$) crosses the centre of the solid rod and line 2 ($x_2/M=3.3$) is centred between lines 1 and 3, as shown in figure 15.

Along the three lines, the turbulence activity of a jet-like flow, the shear layer and wake region of rod are monitored, respectively. In figure 16(*a–c*), the development of longitudinal and transverse mean velocities and the turbulence kinetic energy along the selected lines are plotted. The comparison of the mean velocity curves and the turbulence kinetic energy curves in the vicinity of the grid show clearly the generation of turbulence by a static grid: the mean velocity gradient between the accelerated jet-like flow and backflow at the wake of the obstacle augments the production term (II) in (4.1). As a result, the turbulence kinetic energy reaches its maximum in the wake of the rod (line 3) and has the lowest value always downstream of the open area (line 1). Nevertheless, the gradients of lateral and transverse mean velocities decrease in a very short distance. Thus, according to figure 16 and (4.1), turbulence is no longer produced for $x_1/M > 4$, but it is only transported, diffused and dissipated.

We have extracted each term on the right-hand side of turbulence kinetic energy (see 4.1) along the three lines in figure 17(*a–c*). Along all the lines, the production is active only in the vicinity of the grid, $x_1/M < 4$, and the turbulent transport term is negligibly minute over the complete domain. In the present simulations, Re_λ was not higher than 100 (see table 1), hence the generated turbulence can be accepted to be weak (Mydlarski & Warhaft 1996) and the very low level of the turbulent transport term can be attributed to this weakness. The dissipation term shows a gradual increase up to $x_1/M \approx 3$ and a gradual decrease in the whole downstream region. The viscous diffusion oscillates about zero up to $x_1/M \approx 3$. The amplitude of viscous diffusion increases up to $x_1/M \approx 2$ and decreases gradually in its negative amplitude. In general, the peak locations of dissipation and viscous diffusion lag the peak of the production term, the dissipation peak being the last. For $5 < x_1/M < 10$, dissipation and viscous diffusion are almost at the same level. At the far downstream region ($x_1/M > 20$), viscous diffusion becomes much higher than the dissipation, except for line 1, but with a very low amplitude. Moreover, due to the low levels of turbulence kinetic energy and high Reynolds number of the bulk flow, the diffusion time-scale becomes much smaller than the convective flow. In other words, for complete homogenization via diffusion, the time required is longer than what one can observe in the laboratory. Hence, the reason for the inhomogeneous turbulence field in the far downstream region can be expressed as follows: fast homogenization of the mean velocity field causes a rapid drop in production and, consequently, the dissipation and viscous diffusion processes, so that the generated inhomogeneity of the turbulence field does not have the means of homogenization rather than complete dissipation.

5. Conclusions, final remarks and outlook

The present investigations on grid-generated turbulence showed that turbulence generated by static grids remains spatially inhomogeneous even far downstream of the grid. In both the experimental and the DNS investigations, the lateral profiles of the $\overline{u_1u_1}$ and $\overline{u_2u_2}$ components showed an inhomogeneous field consisting of elongated positive and negative regions standing at rest in space and coalescing with each other. Measurements performed in the mesh Reynolds number range, 4000–8000, did not reveal any dependence of inhomogeneity on the grid Reynolds number.

Furthermore, the numerical investigations revealed that turbulence remains inhomogeneous independent of the porosity of the grid. In the simulations, it was observed that the inhomogeneity of mean velocities decreases very fast behind the symmetric grid, in contrast to the experimentally observed elongated strips of mean velocity. With a simulation performed with a non-uniform grid, it was proved that imperfections in the grid geometry can cause unexpected inhomogeneous mean velocity distributions.

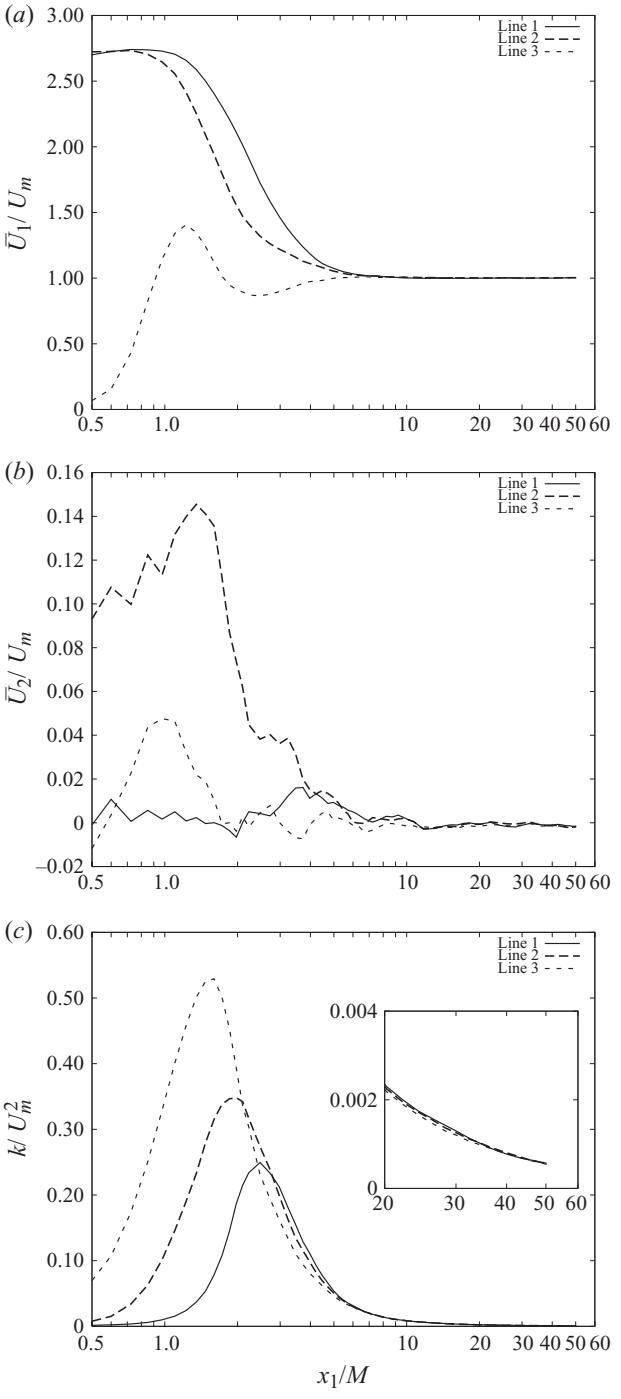

FIGURE 16. Development of (*a*) mean longitudinal velocity normalized by U_m, (*b*) mean transverse velocity normalized by U_m, (*c*) turbulence kinetic energy velocity normalized by U_m^2 for the simulation case at $Re_M = 1400$ with a grid porosity of 53 % (see figure15 for the location of the lines).

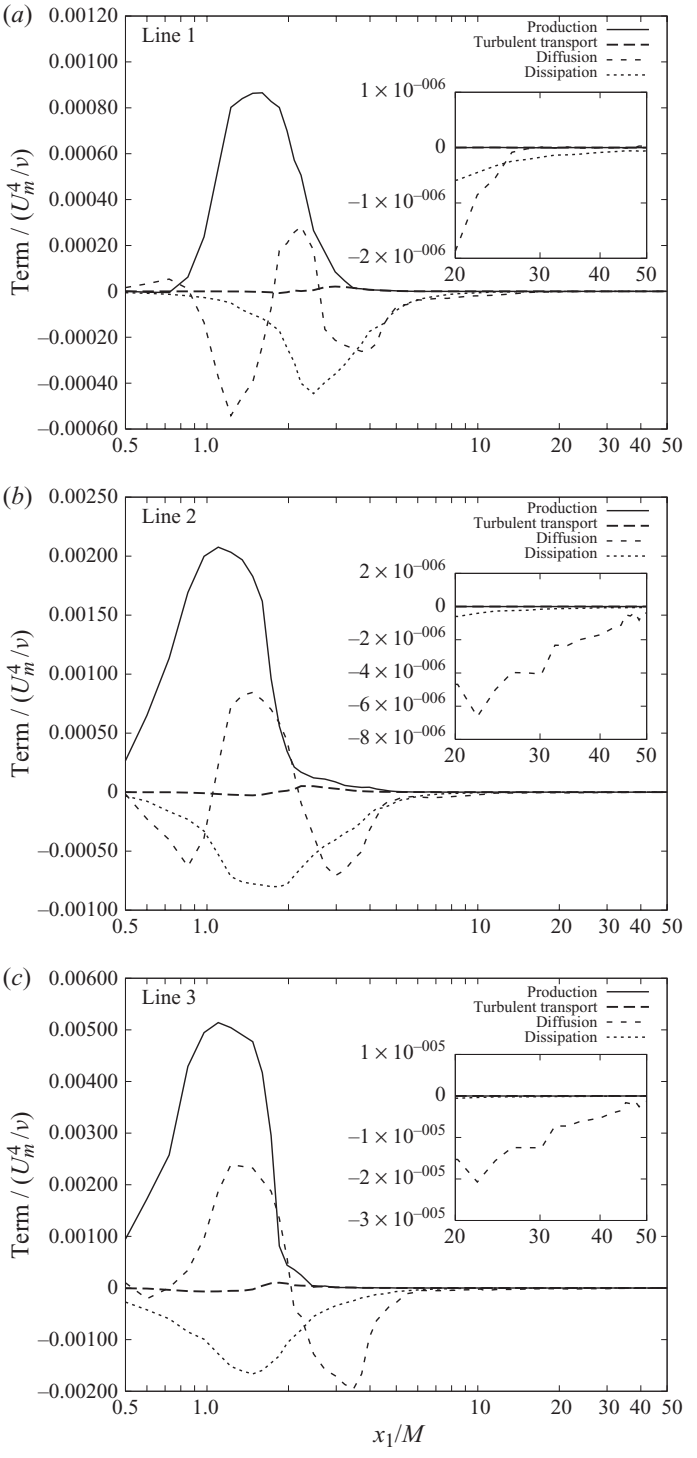

FIGURE 17. Development of the terms in the turbulence kinetic energy equation (4.1) along for the simulation case at $Re_M = 1400$ with a grid porosity of 53 % (*a*) line 1, (*b*) line 2 and (*c*) line 3 (see figure 15 for the location of the lines).

Although the inhomogeneity of mean velocities decreases rapidly behind the symmetric grid, the inhomogeneity of Reynolds stresses persists even afterwards. The analysis of the transport equation for the turbulence kinetic energy, interestingly, showed that fast decay of mean velocity gradients, i.e. decay of spatial inhomogeneity, is the cause of the persistence of inhomogeneity far downstream of the grid. As a result of the decreasing mean velocity gradients, the turbulence production rapidly becomes inactive, so that the large-scale mixing process stops and the remaining viscous diffusion term is insufficient for the turbulence to become homogeneous before it decays completely.

The findings on the inhomogeneity of decaying grid-generated turbulence are in accordance with those of Grant & Nisbet (1957) and show the dependence of measured mean quantities on the relative position of the measurement location with respect to the grid. The presented results demonstrate in detail that even far downstream of the static grid a certain amount of inhomogeneity persists. In other words, obeying all the rules suggested in the literature and discussed here, which were followed in the past by many researchers, does not necessarily lead to a homogeneous turbulence field downstream of static grids. Any kind of study which does not take this fact into consideration can be misleading. For example, in a further study, we aim to show the relevance of this work to the discrepancy observed in the decay constants evaluated from grid-decay experiments. In the present work, no measures were undertaken to generate a more homogeneous turbulence; instead, measured and simulated data were analysed with respect to spatial inhomogeneity. However, it is our expectation that increased mixing action about the turbulence generator and a reduction in the anisotropy of turbulence may enhance the homogeneity of the Reynolds stresses. Increased mixing action can be achieved, for example, by an active grid (Mydlarski & Warhaft 1996). Nevertheless, the available homogeneity measurements downstream of such grids are rather scarce.

The authors gratefully acknowledge the scholarships provided to Özgür Ertunç by the Scientific and Technological Research Council of Turkey and the Bavarian Research Foundation for his PhD studies at FAU LSTM-Erlangen. Without the financial support of LSTM-Erlangen and the Volkswagen Foundation for the construction of the experimental facilities, this study would not have been possible. We would like to thank Professor Hassan M. Nagib for providing us the results of his research on turbulence manipulators.

REFERENCES

Batchelor, G. K. 1953 *The Theory of Homogeneous Turbulence*. Cambridge University Press.

Batchelor, G. K. & Stewart, R. W. 1950 Anisotropy of the spectrum of turbulence at small wavenumbers. *Q. J. Mech. Appl. Math.* **3**, 1.

Batchelor, G. K. & Townsend, A. A. 1948*a* Decay of isotropic turbulence in the initial period. *Proc. R. Soc.* A **193**, 539–558.

Batchelor, G. K. & Townsend, A. A. 1948*b* Decay of isotropic turbulence in the final period. *Proc. R. Soc.* A **194**, 527–543.

Batchelor, G. K. & Townsend, A. A. 1949 The nature of turbulent motion at large wavenumbers. *Proc. R. Soc.* A **199**, 238–255.

von Bohl, J. G. 1940 Das Verhalten paralleler Luftstrahlen. *Ing. Arch.* **11** (4), 295–314.

Bradshaw, P. 1964 Wind tunnel screens: flow instability and its effect on aerofoil boundary layers. *J. R. Aeronaut. Soc.* **68**, 198.

Bradshaw, P. 1965 The effect of wind-tunnel screens on nominally two-dimensional boundary layers. *J. Fluid Mech.* **22** (4), 679–687.

Bradshaw, P. 1971 *An Introduction to Turbulence and Its Measurement*. Pergamon.

Brenner, G., Zeiser, T., Beronov, K., Lammers, P. & Bernsdorf, J. 2003 Lattice Boltzmann methods: high performance computing and engineering applications. In *Parallel Computational Fluid Dynamics* pp. 3–12. Elsevier.

Breuer, M. 2001 Direkte numerische Simulation und Large-Eddy Simulation turbulenter Strömungen auf Hochleistungsrechner. PhD thesis, Friedrich Alexander Universität Erlangen-Nürnberg, LSTM-Erlangen, Germany.

Breuer, M., Bernsdorf, J., Zeiser, T. & Durst, F. 2000 Accurate computations of the laminar flow past a square cylinder based on two different methods: Lattice-Boltzmann and finite volume. *Intl J. Heat Fluid Flow* **21**, 186–196.

Choi, K.-S. & Lumley, J. L. 2001 The return to isotropy of homogeneous turbulence. *J. Fluid Mech.* **436**, 59–84.

Comte-Bellot, G. & Corrsin, S. 1966 The use of a contraction to improve the isotropy of grid-generated turbulence. *J. Fluid Mech.* **25**, 657.

Comte-Bellot, G. & Corrsin, S. 1971 Simple Eulerian time-correlation of full- and narrow-band velocity signals in grid-generated, 'isotropic' turbulence. *J. Fluid Mech.* **48**, 273–337.

Corrsin, S. 1944 Investigation of the behaviour of parallel two-dimensional air jets. *Tech. Rep.* ACR-4H24. NACA.

Corrsin, S. 1963 *Turbulence: Experimental Methods*, vol. 8. Springer.

Djenidi, L. 2006 Lattice-Boltzmann simulation of grid-generated turbulence. *J. Fluid Mech.* **552**, 13–35.

Ertunç, Ö. 2007 Experimental and numerical investigations of axisymmetric turbulence. PhD thesis, Friedrich Alexander Universität Erlangen-Nürnberg, LSTM-Erlangen, Germany. http://www.opus.ub.uni-erlangen.de/opus/volltexte/2007/537/.

Ertunç, Ö. & Durst, F. 2008 On the high contraction ratio anomaly of axisymmetric contraction of grid-generated turbulence. *Phys. Fluids* **20**, 025103.

Ferchichi, M. & Tavoularis, S. 2000 Reynolds number effects on the fine structure of uniformly sheared turbulence. *Phys. Fluids* **12**, 2942–2953.

Freund, H., Zeiser, T., Huber, F., Klemm, E., Brenner, G., Durst, F. & Emig, G. 2003 Numerical simulations of single-phase reacting flows in randomly packed fixed-bed reactors and experimental validation. *Chem. Engng. Sci.* **58**, 903–910.

Fröhlich, J. 2006 *Large Eddy Simulationen turbulenter Strömungen.* B.G-Teubner.

Gence, J. N. 1983 Homogeneous turbulence. *Annu. Rev. Fluid Mech.* **15**, 201–222.

Gence, J. N. & Mathieu, J. 1979 On the application of successive plain strains to grid-generated turbulence. *J. Fluid Mech.* **93**, 501–513.

Gence, J. N. & Mathieu, J. 1980 The return to isotropy of an homogeneous turbulence having being submitted to two successive plane strains. *J. Fluid Mech.* **101**, 555–566.

Grant, H. L. & Nisbet, I. C. T. 1957 The inhomogeneity of grid turbulence. *J. Fluid Mech.* **2**, 263–272.

Hinze, J. O. 1975 *Turbulence*, 2nd edn. New York: McGraw-Hill.

von Kármán, T. 1937 The fundamentals of the statistical theory of turbulence. *J. Aero. Sci.* **4** (4), 131–139.

von Kármán, T. & Howarth, L. 1938 On the statistical theory of isotropoic turbulence. *Proc. R. Soc.* A **164** (917), 192–215.

Kolmogorov, A. N. 1941*a* The local structure of turbulence in incompressible viscous fluid for very large Reynolds numbers. *C. R. Acad. Sci., U.S.S.R.* **30**, 301–305.

Kolmogorov, A. N. 1941*b* Dissipation of energy in locally isotropic turbulence. *C. R. Acad. Sci. U.S.S.R.* **32**, 16–18.

Lammers, P. 2004 Direkte numerische simulationen wandgebundener stroemungen kleiner Reynoldszahlen mit dem Lattice Boltzmann verfahren. PhD thesis, Friedrich Alexander Universität Erlangen-Nürnberg, LSTM-Erlangen, Germany.

Lavoie, P., Djenidi, L. & Antonia, R. A. 2007 Effects of initial conditions in decaying turbulence generated by passive grids. *J. Fluid Mech.* **585**, 395–420.

Liu, R., Ting, D. S.-K. & Rankin, G. W. 2004 On the generation of turbulence with a perforated plate. *Exp. Therm. Fluid Sci.* **28**, 307–316.

Loehrke, R. I. & Nagib, H. M. 1972 Experiments on management of free stream turbulence. *Tech. Rep.* 598. AGARD.

Mazellier, N. & Vassilicos, J. C. 2008 The turbulence dissipation constant is not universal because of its universal dependence on large-scale flow topology. *Phys. Fluids* **20**, 015101.

Mills, R. R. & Corrsin, S. 1959 Effect of contraction on turbulence and temperature fluctuations generated by a warm grid. *Tech. Rep.* 5-5-59W. NASA Memorandum.

Mohamed, M. S. & Larue, J. C. 1990 The decay power law in grid-generated turbulence. *J. Fluid Mech.* **219**, 195–214.

Mydlarski, L. & Warhaft, Z. 1996 On the onset of high Reynolds number grid-generated wind tunnel turbulence. *J. Fluid Mech.* **320**, 331–368.

Naudascher, E. & Farell, C. 1970 Unified analysis of grid turbulence. *J. Engng Mech. Div., ASCE* **96** (No. EM2, Proc. Paper 7214), 121–141.

Özyilmaz, N. 2003 Turbulence statistics in the inner layer of two-dimensional channel flow. Master's thesis, Friedrich Alexander Universität Erlangen-Nürnberg, LSTM-Erlangen, Germany.

Prandtl, L. 1932 Herrstellung Einwand freier luftströme im windkanäle. *Handbuch der Experimentalphysik* [Translated as NACA-TM-726 (1933)] **4** (2), 73.

Prandtl, L. 1933 Attaining a steady air stream in wind tunnels. *Tech. Rep.* NACA-TM-726.

Reynolds, A. J. & Tucker, H. J. 1975 The distortion of turbulence by general uniform irrotational strain. *J. Fluid Mech.* **68**, 673–693.

Sagaut, P. & Cambon, C. 2008 *Homogeneous Turbulence Dynamics*. Cambridge University Press.

Shen, X. & Warhaft, Z. 2000 The anisotropy of the small scale structure in high Reynolds number ($r_\lambda \approx 1000$) turbulent shear flow. *Phys. Fluids* **12** (11), 2976–2989.

Shen, X. & Warhaft, Z. 2002 Longitudinal and transverse structure functions in sheared and unsheared wind-tunnel turbulence. *Phys. Fluids* **14** (1), 370–381.

Sjögren, T. & Johansson, A. V. 1998 Measurement and modelling of homogeneous axisymmetric turbulence. *J. Fluid Mech.* **374**, 59–90.

Spalart, P. 1988 Direct numerical study of leading edge contamination. In *Fluid Dynamics of Three-dimensional Turbulent Shear Flows and Transition*, pp. 5.1–5.13.

Succi, S. 2001 *The Lattice Boltzmann Equation: For Fluid Dynamics and Beyond*. Oxford University Press.

Tan-Atichat, J. & Nagib, H. M. 1982 Interaction of free-stream turbulence with screens and grids: a balance between turbulence scales. *J. Fluid Mech.* **114**, 501–528.

Tan-Atichat, J., Nagib, H. M. & Drubka, R. E. 1980 Effects of axisymmetric contractions on turbulence of various scales. *Tech. Rep.* 165136. NASA Contractor Report.

Taylor, G. I. 1935*a* Statistical theory of turbulence. Parts 1–4. *Proc. R. Soc.* A **151**, 421.

Taylor, G. I. 1935*b* Turbulence in a contracting stream. *Z. Angew. Math. Mech.* **15**, 91–96.

Taylor, G. I. 1937 The statistical theory of isotropic turbulence. *J. Aero. Sci.* **4**, 311.

Taylor, G. I. 1938 The spectrum of turbulence. *Proc. R. Soc.* A **164**, 476.

Townsend, A. A. 1954 The uniform distortion of homogeneous turbulence. *Q. J. Mech. Appl. Math.* **7**, 104–127.

Tucker, H. J. & Reynolds, A. J. 1968 The distortion of turbulence by irrotational strain. *J. Fluid Mech.* **32**, 657–673.

Uberoi, M. S. 1956 Effect of wind-tunnel contraction on free-stream turbulence. *J. Aero. Sci.* **23**, 754–764.

Uberoi, M. S. 1957 Equipartition of energy and local isotropy in turbulent flows. *J. Appl. Phys.* **28** (10), 1163–1170.

Warhaft, Z. 1980 An experimental study of the effect of uniform strain on thermal fluctuations in grid-generated turbulence. *J. Fluid Mech.* **99**, 545–573.

Warhaft, Z. & Shen, X. 2002 On the higher order mixed structure functions in laboratory shear flow. *Phys. Fluids* **14** (7), 2432–2438.

Wellein, G., Zeiser, T., Hager, G. & Donath, S. 2006 On the single processor performance of simple Lattice Boltzmann kernels. *Comput. Fluids* **35**, 910–919.

Wolf-Gladrow, D. 2000 *Lattice-Gas Cellular Automata and Lattice Boltzmann Models: An Introduction*. Springer.

Zeiser, T., Lammers, P., Klemm, E., Bernsdorf, J. & Brenner, G. 2001 CFD-calculation of flow, dispersion and reaction in a catalyst filled tube by the lattice Boltzmann method. *Chem. Engng Sci.* **56**, 1697–1704.